Deformation and frictional failure of granular media in 3D analog and numerical experiments

P.I. Ioannidi[1,2*+], S. McLafferty[1+], J.E. Reber[1], G. Morra[3], D. Weatherley[4]

[1] Department of Geological and Atmospheric Sciences, Iowa State University, Ames, IA, USA

[2] now at Department of Earth Sciences, Vrije Universiteit Amsterdam, Amsterdam, The Netherlands

[3] Department of Physics, University of Louisiana at Lafayette, Lafayette, LA, USA

[4] Julius Kruttschnitt Mineral Research Centre, Sustainable Minerals Institute, The University of Queensland, Brisbane, Australia

* Corresponding author (email: ioannidi@iastate.edu)

+ both authors contributed equally to this study.

Keywords: granular media, frictional failure, grain comminution, analog experiments, Discrete Element Method

Acknowledgements: PII, SMcL, JER, GM have been supported through National Science Foundation CAREER award #1843676.

This is a non-peer reviewed preprint that has been submitted to Pure and Applied Geophysics (PAGEOPH).

Abstract

Frictional sliding along grain boundaries in brittle shear zones can result in the fragmentation of individual grains, which ultimately can impact slip dynamics. During deformation at small scales, stick-slip motion can occur between grains when existing force chains break due to grain rearrangement or failure, resulting in frictional sliding of granular material. The rearrangement of the grains leads to dilation of the granular package reducing the shear stress and subsequently leading to slip. Here, we conduct physical experiments employing HydroOrbs, an elasto-plastic material, to investigate grain comminution in granular media under simple shear conditions. Our findings demonstrate that the degree of grain comminution is dependent on both the normal force and the size of the grains. Using the experimental setup, we benchmark Discrete Element (DE) numerical models, which are capable of simulating the movement, rotation, and fracturing of elasto-plastic grains subjected to simple shear. The DE models successfully replicate both grain comminution patterns and horizontal force fluctuations observed in our physical experiments. They show that increasing normal forces correlate with higher horizontal forces and more fractured grains. The ability of our DE models to accurately reproduce experimental results opens up new avenues for investigating various parameter spaces that may not be accessible through traditional laboratory experiments, for example in assessing how internal friction or cohesion affect deformation in granular systems.

1 Introduction

In the upper crust, brittle deformation in shear zones is recorded in the fracturing of rocks and the formation of fault rocks such as gouge (Sibson, 1977). In brittle fault zones, cataclasis leads to grain size reduction due to frictional sliding along grain boundaries and fragmentation of individual grains within the shear zone (Sibson, 1977; Marone & Scholz, 1989). Frictional sliding can result in a stick-slip signal where stress builds during sticking events and is subsequently released after the strength of the rock is overcome and displacement occurs (Brace & Byerlee, 1966). At small scales, stick-slip motion can occur between grains during deformation while at large scales, stick-slip motion between volumes of rock can lead to earthquakes.

In any granular system, stick-slip motion can be linked to the formation and failure of force chains. In a jammed state (the sticking phase), forces are supported by force chains (Cates et al., 1998). During this phase, shear stress increases until grains begin to rearrange or break initiating the slipping phase. Slip occurs when existing force chains break due to grain rearrangement or failure, resulting in frictional sliding of the granular material.

The rearrangement of the grains leads to dilation of the granular package reducing the shear stress, subsequently leading to slip (Cain et al., 2001).

Numerous experimental and numerical studies have investigated deformation dynamics of granular systems during shear deformation in 2-dimensions (2D) and 3-dimensions (3D) (e.g., Daniels & Hayman, 2008; Mair et al., 2002; Frye & Marone, 2002; Reber et al., 2015; Ladd & Reber, 2020; Siman-Tov & Brodsky, 2018), showing that the deformation of a granular system is directly affected by grain comminution, grain shape, roughness, and particle size distribution (e.g., Marone and Scholz, 1989; Mair et al., 2002). The particle size distribution and particle friction in a deforming 2D granular system impacts the formation of particle bridges where high differential stresses are created leading to breaking of individual particles due to particle rolling (Morgan and Boettcher, 1999). Another mechanism leading to grain comminution is the rearrangement of grains close to any shear boundary during deformation (Siman-Tov & Brodsky, 2018). Numerical experiments on 3D granular systems show that the grain size distribution is a direct function of accumulated strain and applied normal stress (Abe and Mair, 2005). Guo and Morgan (2006) simulated the comminution process of quartz gouge and examined the influence of grain comminution on the frictional and micromechanical behavior of granular shear zones. Their results show that grain comminution can decrease or increase gouge strength, depending on the direction and degree of change in grain shape. In addition, they show that the intensity and probability of grain comminution in narrow grain size gouges are affected by grain shape, material strength, and normal stress. Homogeneous grain size distributions in a deforming granular system will gradually evolve into a wider grain size distribution (Mair and Abe, 2008). Two distinct comminution mechanisms, grain splitting and grain abrasion, that are favored for different normal stresses and wall roughness, are responsible for the evolution in grain sizes in granular systems (Mair and Abe, 2011). With an increase in wall roughness, the frictional strength of the system increases and eventually becomes independent of roughness (Shojaaee et al., 2012).

Here, we explore grain comminution in granular media from the perspective of both laboratory and numerical experiments. We present experiments using a new experimental material, HydroOrbs. HydroOrbs are elastic until an elastic yield point is reached and they fracture and split into smaller pieces. Their original size and elastic yield can be tuned, which makes them a good target material for experiments on grain comminution. We use the experimental setup and results to benchmark Discrete Element (DE) numerical models, which in future steps will allow for an investigation of the parameter space not accessible through physical experiments. In both the physical and the numerical experiments, we deform particles that fracture in simple shear. We use the material and geometrical parameters from the physical experiments as input parameters for the DE models. We show that the DE experiments can reproduce qualitatively grain comminution and particle migration as well as the horizontal force fluctuations of the physical experiments.

2 Physical experiments

We conduct a series of granular experiments in a ring shear apparatus where we deform elasto-plastic HydroOrbs. We systematically change the imposed normal force and monitor the failure of individual grains and the deformation dynamics.

2.1 Experimental setup and materials

Experiments are conducted in a ring shear apparatus consisting of two concentric cylinders with radii of 11 cm and 19 cm attached to a baseplate. The experimental material is contained in the resulting 8 cm cylindrical annulus at a height of 16 cm. The experimental chamber is capped by a hydraulic lid that allows for control of the normal force acting on the experimental material. Shear of the experimental material is initiated by rotating the baseplate and experimental chamber walls, while keeping the lid stationary. Both the lid and the baseplate of the experimental chamber have 1 cm high teeth that span the width between the experimental walls to increase the contact area with the experimental material and to transfer the deformation motion. A cylindrical stepper motor mounted around the base of the experimental chamber drives the experimental chamber. The motor is connected to the experimental chamber via a spring that is connected to a force gauge. Adding the spring as an elastic element between the motor and the experimental chamber allows for distinct stick slip and force oscillations to occur (Daniels and Hayman, 2009; Reber et al., 2014; Birren and Reber 2019). We use a spring with spring constant of 9712 N/m for all experiments. The pulling force necessary to rotate the experimental chamber is recorded at a rate of 10 Hz, and an average bulk force is calculated for every full rotation of the experimental chamber. The force signal from the deforming material is separated from the machine noise with a moving average filter. To achieve this, the difference between the raw data and noise filter is calculated at every data point. Then, the variance of the difference values is calculated for each rotation. Larger differences between the raw data and filtered data result in larger variance values. This reflects a stronger oscillation of the spring due to the deforming experimental materials. In addition to the pulling force, we measure the normal force applied to the experimental materials with a force gauge mounted to the lid of the apparatus. For a more detailed description of the experimental setup, removal of background noise, and pulling force data treatment see McLafferty et al. (2023).

HydroOrbs or Hydrogel spheres (e. g., Dijksman et al., 2017; James et al., 2020) are used as granular experimental material. HydroOrbs are small, dehydrated spheres (~ 2 mm in diameter with larger spheres ~ 4 mm) that once in contact with water swell to about ten times their size. Both colorless and colorful HydroOrbs are used in the physical experiments and the orbs expand to different sizes depending on the salinity of the water when submerged (Table 1 and Supplemental Table 3). The colorless and colorful orbs grow to average diameters of 1.69 cm and 1.66 cm, respectively, when placed in deionized (DI) water, and 1.41 cm and 1.43 cm, respectively, when placed in tap water. Very large colorful orbs resulting from larger dehydrated spheres (~ 4 mm) are also used in experiments and have an average diameter of 3.87 cm after being placed in tap water (Table 1 and Supplemental Table 3). HydroOrb size is the only physical parameter that is significantly different between orbs (colorless and colorful) made with DI water, orbs made with tap water, and large orbs (Supplemental Table 3).

We soak the HydroOrbs in water for at least 24 hours before the start of an experiment to ensure maximum hydration. The fully hydrated orbs deform in a linear elastic manner (Dijksman et al., 2017) until they reach a yield point after which they fracture into smaller pieces (James et al., 2020). The average yield stresses of the orbs are ~15 kPa for the large orbs, and between ~72 and ~78 kPa for colorless small orbs soaked in DI and tap water, respectively, with relatively wide standard deviations (Supplemental Table 3). To reduce the average yield stresses and standard deviations of the orbs, we puncture the HydroOrbs perpendicular to the outer edge of the orbs towards the center with a 24-gauge sewing pin (diameter 0.55 mm). The puncture length to orb diameter ratio is 0.4 for all orb types. The puncture introduces a line of weakness and is needed to penetrate a rind of denser material in the outermost 1-2 mm of the orb (Chang et al., 2018). This line of weakness leads to decreased yield stresses of ~25 kPa for the colorless and colorful orbs made with DI water, while the colorless and colorful orbs made with tap water have yield stresses of ~21 kPa, and the large orbs have a yield stress of ~7 kPa. Note, all HydroOrb types have yield stresses that overlap when taking standard deviation into consideration. A comprehensive list of orb physical properties can be found in Supplemental Table 3.

2.2 Results from laboratory shear experiments

Laboratory experiments are conducted with both the colorless and colorful HydroOrbs including the large orbs for a total of six experiments. The HydroOrbs are punctured before every experiment and only one type of orb is placed in the ring shear apparatus for each experiment. Experiments CL_D1 and CL_D2 use colorless DI water orbs while experiment and CL_T uses tap water orbs. Experiments CF_D and CF_T are repeats of CL_D2 and CL_T, respectively, but with colorful orbs. Experiment CF_LG uses large colorful orbs. The experiments are conducted at average confining pressures between 2.04 and 2.67 kPa with the exception of CL_D1 and CF_LG which are deformed at relatively low confining pressures of 0.82 kPa and 0.89 kPa, respectively. A list of experiments and parameters can be found in Table 1. Each experiment comprises of 10 to 20 rotations of the experimental chamber depending on water leakage out of the ring shear apparatus. Each full rotation takes 330 seconds due to an imposed angular velocity of 0.019 rad/sec (corresponding to an average linear velocity of 0.28 cm/sec) at the baseplate of the experimental chamber. During each experiment, we record the horizontal pulling force and the normal force. In addition, HydroOrb migration and failure is recorded throughout the experiments with two cameras. One camera is mounted to the experimental chamber and rotates with the motor documenting deformation in one location of the experiment. The other camera is stationary and positioned at the outside of the annulus facing towards the center documenting the variability throughout the experiment.

Table 1: Parameters for the analog experiments. All orbs are punctured. CL = Colorless, CF = Colorful, D = DI water, T = Tap water, and LG = Large. The diameters and yield stresses of the orbs used in the experiments are listed including standard deviation. Maximum normal force and confining pressure recorded during the experiment are also listed.

Experiment	Orb Type	Orb Diameter (cm)	Orb Yield Stress (kPa)	Max. Normal Force (N)	Max. Confining Pressure (kPa)
CL_D1	CL/D	1.69 ± 0.09	25.44 ± 13.96	61.56	0.82
CL_D2	CL/D	1.69 ± 0.09	25.44 ± 13.96	154.00	2.04
CL_T	CL/T	1.41 ± 0.06	21.43 ± 13.81	201.27	2.67
CF_D	CF/D	1.66 ± 0.08	25.62 ± 16.27	161.00	2.14
CF_T	CF/T	1.43 ± 0.08	21.97 ± 15.70	165.52	2.20
CF_LG	LG/T	3.87 ± 0.25	7.07 ± 12.79	67.19	0.89

2.2.1 Orb rearrangement and failure

HydroOrb rearrangement is observed in every experiment regardless of confining pressure. Most orb movement takes place in the top half of the experimental chamber in the form of individual or multiple orbs sliding past each other. The orb movement is most prominent close to the shear boundary beneath the top plate. There is little to no orb rearrangement at the bottom of the experimental chamber where the orbs passively move with the bottom plate of the chamber. Instead, these orbs show elastic deformation due to stress imparted from orb rearrangement above. Due to rearrangement, we observe HydroOrbs moving both vertically and horizontally within the experimental chamber. After 5 to 10 rotations, widespread orb rearrangement throughout the height of the experimental chamber lessens and becomes mostly limited to the top half of the chamber as the total volume decreases due to HydroOrb failure.

HydroOrb failure is observed in all experiments except for experiment CL_D1 which was conducted at a lower confining pressure. However, the percentage of broken orbs differs between experiments (Table 2), with the highest percentage of broken orbs in experiment CF_LG, even at a low confining pressure (0.89 kPa), and the lowest percentage of broken orbs in experiment CF_T despite a larger confining pressure (2.20 kPa). Broken orb percentage is larger in the experiments using DI water orbs compared to tap water orb experiments, regardless of whether the orbs are colorful or colorless. HydroOrb failure occurs throughout the height of the material chamber but is most prominent at the shear boundary between the lid of the material chamber and the orbs immediately below. During an experiment we observe downward orb fragment migration from the shear boundary at the top of the experimental chamber towards the middle of the chamber where the fragments fill the voids between unbroken HydroOrbs. However, fragments do not migrate all the way to the bottom of the material chamber, instead they stop a few centimeters above the bottom plate to create a band of fragments in the middle of the experimental chamber (Fig. 1). The thickness of the fragment band increases throughout the experiment as more orbs break at the top of the chamber. The band of fragments reaches a finite thickness during an experiment after HydroOrb failure stops and fragments are no longer supplied from the shear boundary. Once the supply of fragments stops, the thickness of the fragment band decreases as the fragments consolidate (Fig. 1). This consolidation happens in experiments CL_D2, CF_D, and CF_LG after orbs are no longer observed to fail at the shear boundary. The fragment band formation and consolidation are less apparent in experiments CL_T and CF_T where smaller tap water orbs are used. Table 2 summarizes the final fragment band location and thickness for each experiment. Notably, fragment band thickness decreases with increasing orb size used in the experiment (Table 2). For example, experiments involving small tap water HydroOrbs (Fig.

2c and e) result in a fragment band thickness of 5.5 to 6.5 cm (CL_T and CF_T, respectively), whereas experiments with DI orbs (Fig. 2b and d) result in fragment band thickness of 4 to 4.5 cm (CF_D and CL_D2, respectively). CF_LG (Fig. 2f) results in the thinnest band of fragments at 3.5 cm (Table 2). The reason could be that fragment formation slows down or stop around rotations 7 to 10 for the large and DI orbs so no more fragments are supplied from the top. The fragment band then compacts due to orb movement at the top pushing the fragments downward while the bottom of the fragment band stays at the same height (due to no orb rearrangement below).

Table 2: List of physical experiment parameters including the percent of broken HydroOrbs and the bottom and top height of the fragment band in the material chamber, respectively.

Experiment	% Orbs Broken	Final Fragment Band Location (Average height in cm)	Average Orb Diameter (cm)
CL_D1	0	-	1.69 ± 0.09
CL_D2	16.2	4.5 – 9	1.69 ± 0.09
CL_T	6.4	5 – 10.5	1.41 ± 0.06
CF_D	18.9	4 – 8	1.66 ± 0.08
CF_T	2.7	4 – 10.5	1.43 ± 0.08
CF_LG	21.1	6 – 9.5	3.87 ± 0.25

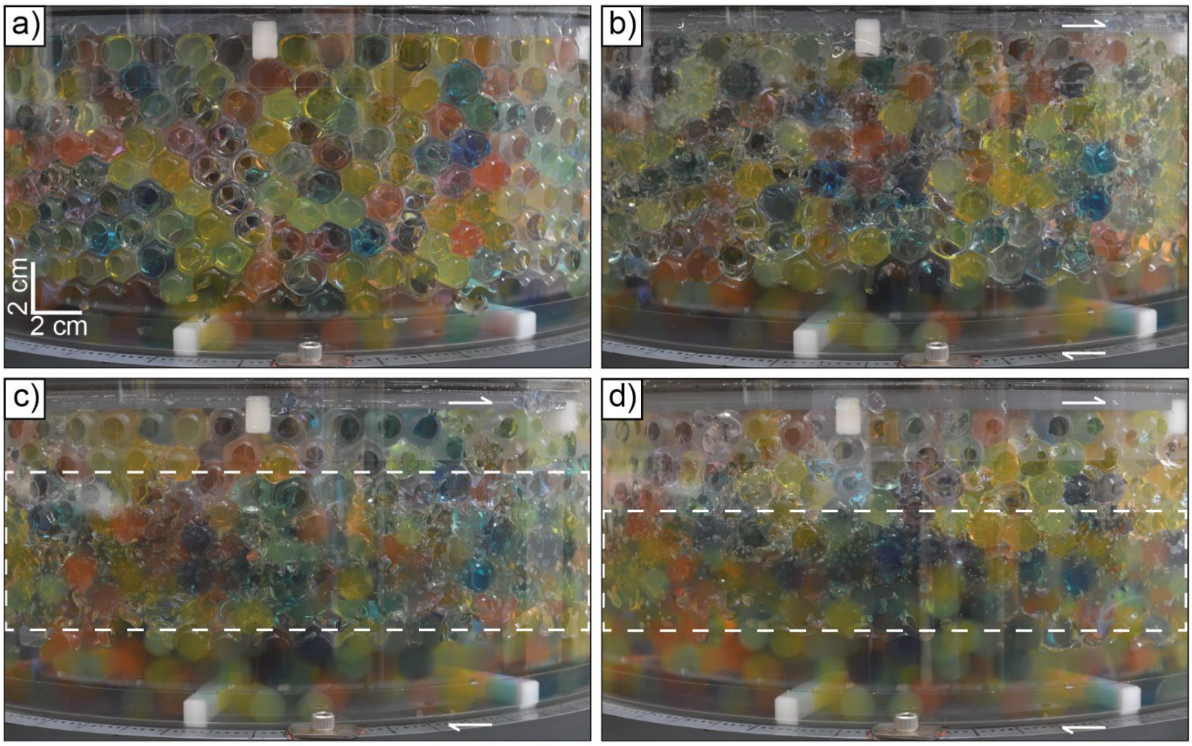

Fig. 1 *Photos of experiment CF_D taken from the outside of the experimental chamber looking towards the smaller cylinder at the center of the chamber. a) HydroOrbs before the experiment, b) after rotation 5, c) after rotation 10, and d) after the final rotation. Dashed boxes in c and d encompass the fragment bands. Note the decrease in height of the fragment band between rotation 10 (c) and after the final rotation (d)*

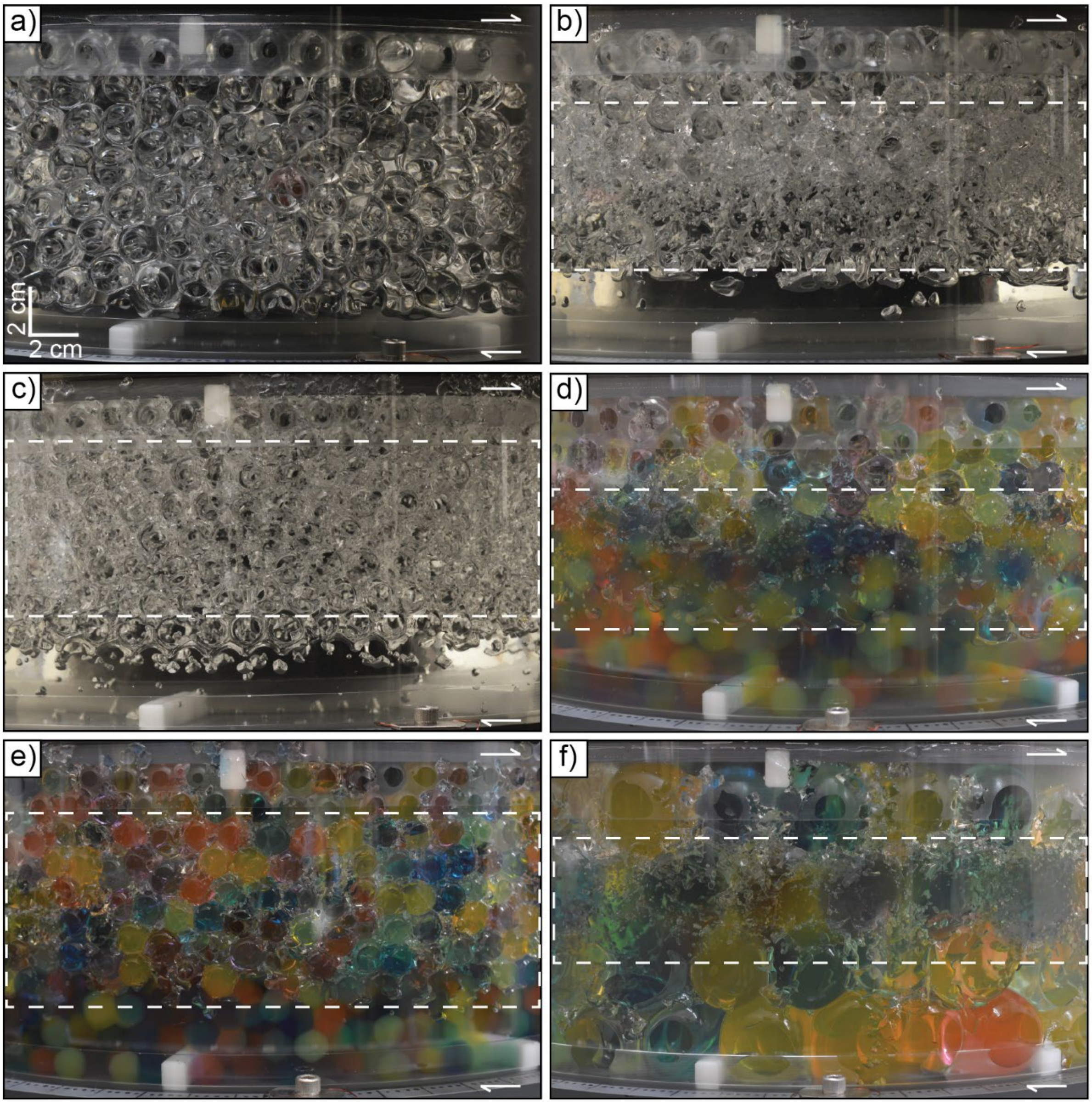

Fig. 2 *Photos of the physical experiments after the last rotation, taken from the outside of the material chamber looking toward the inner cylinder. a) CL_D1, b) CL_D2, c) CL_T, d) CF_D, e) CF_T, and f) CF_LG. Fragment band location noted with dashed box. Note the absence of fragment band in a) due to the absence of fracturing*

2.2.2 Force measurements

The pulling force magnitude and its variance calculated from experiments mirror the observations of orb rearrangement and failure discussed above. Orb rearrangement is recorded in the force data as large force magnitude oscillations at different frequencies and amplitudes due to the spring boundary condition. These large force oscillations result in relatively greater variance values. Where orb rearrangement is most prevalent at the beginning of the experiments, the pulling force magnitude and variance are at (or close to) their maximum in most experiments (Fig. 3). The pulling force and variance values decrease in magnitude with increasing rotations as HydroOrbs fail. The only exception to the decrease in force magnitude and variance through increasing rotations is CL_D1 where there is orb rearrangement but no orb failure in the presence of a relatively low applied normal force. In CL_D1, the force magnitude and variance values are less than the values from experiments where the applied normal force is greater (Fig. 3).

Most experiments have maximum force magnitudes and variance values in the first rotation. After the first rotation, the force magnitude and variance significantly decrease. Conversely, the last several force magnitude and variance values for each experiment are relatively constant (Fig. 3). To describe the relationship between force magnitude or variance with increasing strain, we fit power law trendlines to the data for all experiments to help guide the eye and make the pattern in the data more visible (Fig. 3). Conversely, where there is no orb failure in CL_D1, there is no decrease in force magnitude and variance values with increasing strain resulting in the poor power law trendline fit.

While the average pulling force magnitudes for different experiments yield different trendlines, the error bars on individual force magnitude points overlap heavily between experiments. In addition, individual variance points overlap between experiments, making it difficult to determine differences (if there are any) in material deformation between the experiments. According to the power law trend, both experiments involving the smallest orbs, CL_T and CF_T, record the largest variance values towards the end of the experiments. Experiments CL_D2 and CF_D record comparable variance values, which are less than those from the tap water orb experiments. The experiment with the largest orbs, CF_LG, records the smallest variance values (except CL_D1) towards the end of the experiment. As HydroOrb size increases, variance at the end of the experiment decreases, which is consistent with less orb rearrangement due to grain failure at the beginning of the experiment. The experiment with the most orb failure is experiment CF_LG (21.1%), which records the lowest variance values at the end. Further, 16.2% of orbs failed in experiment CL_D2 and 18.9% failed in experiment CF_D, corresponding to similarly low variance values towards the end of the experiments.

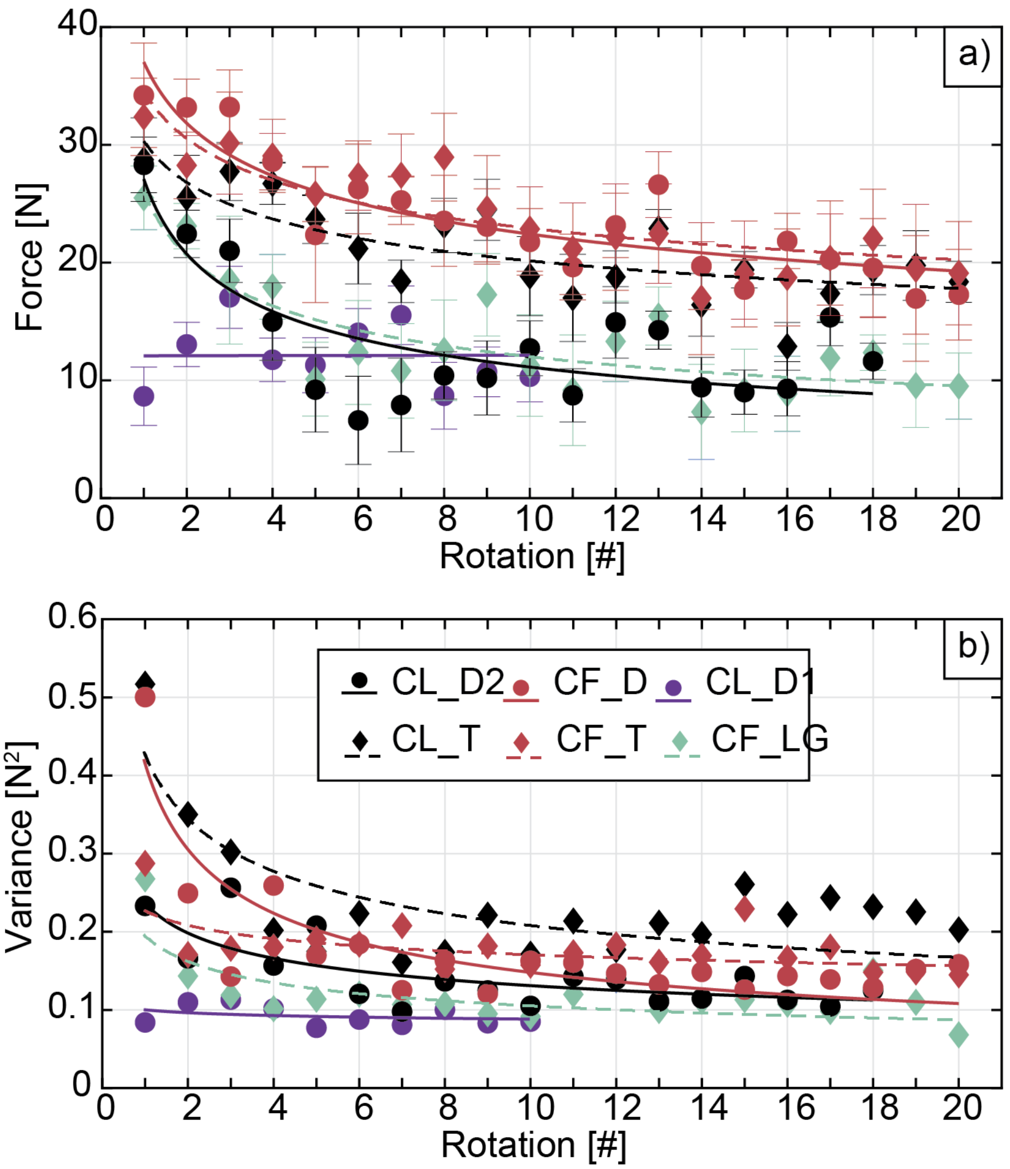

Fig. 3 *Force data results for the experiments with power law trendlines. a) Pulling force magnitude with increasing rotations, b) variance. Note each rotation is completed in 330 seconds. Data are from McLafferty et al., 2023*

2.3 Summary of laboratory shear experiments

Most orb rearrangement and fragment formation (when present in experiments) take place near the top of the experimental chamber. Throughout the experiment, the orb fragments migrate downward to the middle of the experimental chamber to form a fragment band. This brittle failure of the HydroOrbs is recorded in the force gauge data as a decrease in force magnitude and variance. When no orb failure is present, experiment CL_D1, there is little to no decrease in force magnitude and variance.

The confining pressures of most experiments fall within the range of 2.0 to 2.2 kPa and result in no systematic difference in orb failure, force magnitude or variance. However, when considering only one HydroOrb type (such as orbs made with DI water) the confining pressure does play an important role in grain failure, with the lower confining pressure in CL_D1 resulting in no orb failure. As confining pressure increases within the three experiments with DI HydroOrbs, the percentage of broken orbs (Table 2) and pulling force (Fig. 3a) also increase. Alternatively, experiment CF_LG is conducted with a similarly low confining pressure to CL_D1 (~0.9 and ~0.8 kPa, respectively) but results in the highest percentage of orb failure across all experiments. Therefore, when confining pressure is held relatively constant, the orb properties, such as diameter and yield stress, dictate orb failure.

Combining both the visual results and force data from the analog experiments allows us to correlate HydroOrb size and grain comminution. As orb size increases, the percentage of broken orbs also increases, regardless of confining pressure. The fragment band thickness and the force magnitude and variance are also correlated with the size of HydroOrbs. Fragment band width recorded at the end of the experiments decreases with increasing orb size. Finally, the force and variance magnitudes at the end of the experiments are anti-correlated to orb size.

3 Numerical experiments

Numerically, granular media are most often studied by employing the Discrete Element or Lattice Solid methods (Cundall and Strack, 1979; Mora and Place, 1993; 1994; Place and Mora, 1999; Abe et al., 2004; Wang et al., 2006). Both methods simulate systems as an assemblage of discrete particles interacting with each other allowing the tracking of mechanical interactions between particles. There are two common approaches when simulating a granular medium under shear, either as unbonded microparticles (e.g., Morgan and Boettsher, 1999; Mair and Hazzard, 2007; Rathbun et al., 2013), or as bonded assemblages of microparticles, that act as a singular grain (e.g., Mora and Place, 1998; Abe et al., 2002; Mair and Abe, 2008). In both cases, the interactions between the unbonded particles or the bonded grains are governed by frictional laws and elastic interactions by using equations of motion and simplified force-displacement interaction laws (Wang et al., 2006). Here we are using bonded grains to simulate the HydroOrbs, which allows us to monitor fracturing processes and resulting grain fragment mobility.

3.1 Numerical setup and material parameters

To investigate failure and grain comminution in our models, we make use of the parallel DE package ESyS-Particle (Abe et al., 2004; Wang et al., 2006; https://launchpad.net/esys-particle). The numerical solution of particle interactions involves computing the net force acting on each particle at a given time, then updating particle velocities and positions via an explicit finite difference integration scheme. The DE-particles can be bonded together elastically, thus creating bonded macro-particles, which act as a representation of the HydroOrbs in the physical experiments. The breaking of bonded grains results in unbonded (micro-)particles. These unbonded particles can interact with other unbonded micro-particles or with bonded grains via frictional forces. Henceforth, we will refer to grains made of many small particles as (bonded) grains and to the individual unbonded small particles as micro-particles.

The geometry of the numerical simulation resembles the analog ring shear apparatus (see Table 3 for details on analog and DE model dimensions and material parameters). Two unbreakable indented plates encompass the numerical grains (Fig. 4a). Each plate is composed of ca. 30,000 discrete micro-particles. The size of the grooves on the plates matches the laboratory setup (10 mm height. The space between the plates is filled with 116 bonded grains, and each grain is as an aggregate of ca. 900 discrete micro-particles bonded together by breakable elastic bonds (Fig. 4b, inset).

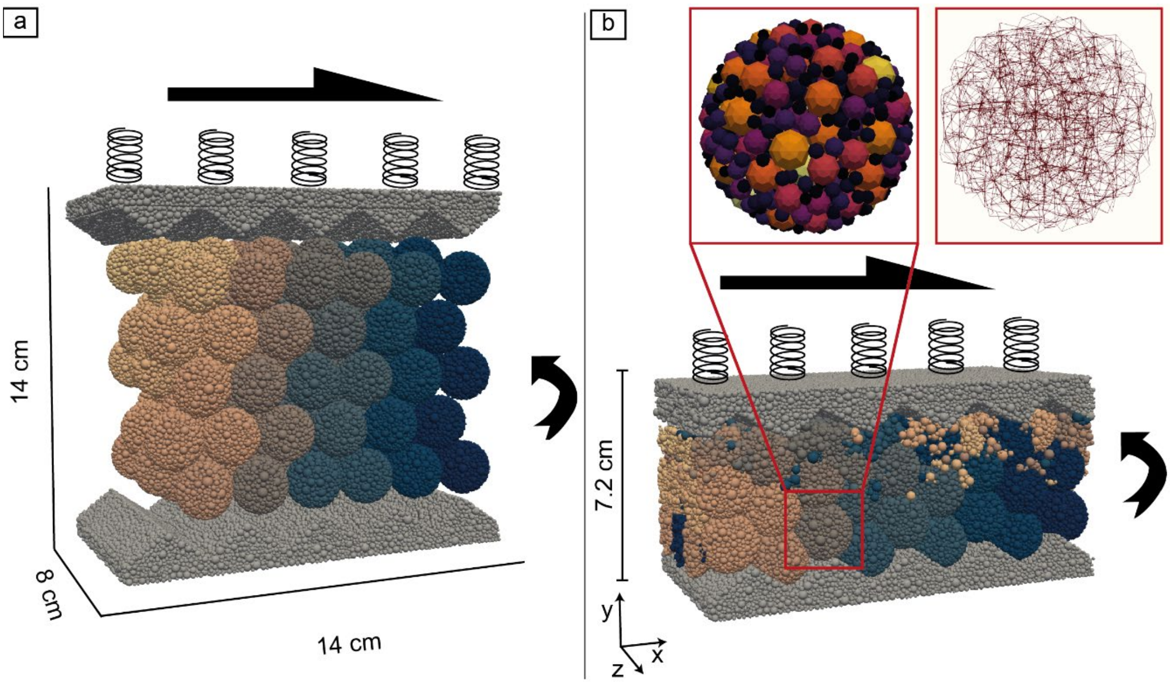

Fig. 4 *Geometry and boundary conditions of the DE models. Colors on the brown to blue color map shows micro-particles that form one bonded grain. Vertical springs denote constant force applied on the moving plate, horizontal arrows correspond the shearing velocity implemented on the moving plate, curved arrow denotes periodic boundary condition along the yz plane. a) Initial geometry of the numerical models. b) geometry at the end of the simulation; insets show one bonded particle, composed of ca. 900 micro-particles (left), elastic bonds between individual micro-particles (right). The black to orange color scale shows micro-particle radii within one bonded grain. Normal force in this model is 38 N. Note the different vertical size of the model in the first step (14 cm; a) versus the final step (ca. 7.2 cm; b)*

The total number of bonds for all micro-particles forming the 116 grains is ca. 320,000. When the bond failure threshold of the micro-particles within a bonded grain is reached, the micro-particle bonds break, and the grains can fracture. The dimensions and material parameters of the bonded grains are chosen to mimic the HydroOrbs (Table 3).

Simulating the full experimental domain would be computationally very expensive; we, therefore, simulate a small section of the domain and use periodic boundary conditions on the left and right vertical boundaries; thus, particles moving out on one side of the domain appear on the other side, without any loss of bonds, velocity etc.

The numerical simulations are characterized by three distinct phases. The first one is the compaction of the grains, achieved by applying constant normal force on one plate (spring in Fig. 4). This phase starts at the beginning of the simulation and normal force is kept constant throughout the simulation. Note that instead of using the same normal force values as in the experiment, we use values that correspond to the same normal stress; since our numerical domain is smaller than the experimental chamber, the numerical normal forces are also smaller (Table 3). Once the grains have been sufficiently compacted and a steady state is achieved, a constant shearing velocity is applied on the top plate, under the same constant normal force. This phase starts at t = 250 s and the shearing velocity increases linearly from zero to a steady velocity at t = 350 s. In the third stage, the shearing velocity is kept constant until the end of the simulation (t ~ 950s). The presented numerical models mimic the setup and material parameters of the physical experiments with the DI water HydroOrbs (CL_D1, CL_D2, and CF_D), which mainly differ in normal force. We complement these numerical models by five additional ones in order to investigate a wider normal force distribution (Table 3). The purpose of the numerical models is to evaluate the effect of normal force on grain comminution and provide data on parameters that cannot be measured in the analog experiments, such as the rate of breaking of bonds during shearing.

We vary the normal force from 8 – 50 N, at 6 N increments while using a very low coefficient of friction ($\mu = 0.05$), to account for the slippery surface of the HydroOrbs forming due to the thin water film that surrounds them. Since we have no measure of the cohesion of the HydroOrbs, we use a value close to the measured yield stress of the HydroOrbs (Tables 1 and 3).

*Table 3: Dimensions, material properties and boundary conditions of analog and numerical experiments. [1]Poisson ratio, [2]friction angle, [3]Young modulus, [4]yield stress, [5]cohesion, [6]coefficient of friction, [7]normal force, [8]shearing velocity. *Circumference of the experimental chamber (or the average distance rotated for one full rotation), **density/mass approximation (see Discussion for details).*

	Dimensions					Materials							Boundary conditions				
	Length (cm)	Height (cm)	Width (cm)	Grain diameter (cm)	DE radius (cm)	Density (kg/m³)	ν^{1}	φ^{2}	Y^{3} (kPa)	$\sigma_y{}^{4}$ (kPa)	Co^{5} (kPa)	μ^{6}	$F_n{}^{7}$ (N)	$v_s{}^{8}$ (cm/s)	Spring constant (N/m)	Timestep (s)	Exp. Time (s)
Analog	94.25*	12.6-13	8	~1.7	-	~ 1	0.39 ±0.07	-	107 – 137	25	-	-	60-161	0.28	9712	1	3300-6600 (10-20 rotations)
DEM	14	14	8	~2.0	0.05 – 0.2	1e6**	0.4	45°	135	-	30	0.05	8-50	0.3	-	1e-3	950-1200

3.2 Numerical Results

3.2.1 Grain re-arrangement and failure

Grain rearrangement is observed in all the numerical experiments, regardless of normal force, similarly to the laboratory experiments. Moreover, most grain movement happens at higher normal forces, and tends to localize along the moving plate, which is where normal force and shearing velocity are applied. At low normal forces (Fig. 5a, b), fewer grains break leading to fewer microparticles, which are mainly located in the upper third of the domain, close to the moving plate. As normal force increases, however, the number of broken grains increases as well (Fig. 5c, d). Notably, microparticles travel until about the middle of the model (Fig. 5c, d top). Finally, vertical velocities increase with normal force (Fig. 5c, d bottom) close to the boundary with the moving plate. Given the absence of gravity in our numerical models, and the fact that compression is applied at the top, the grains are more mobile close to the moving plate while the grains closer to the fixed plate are jammed.

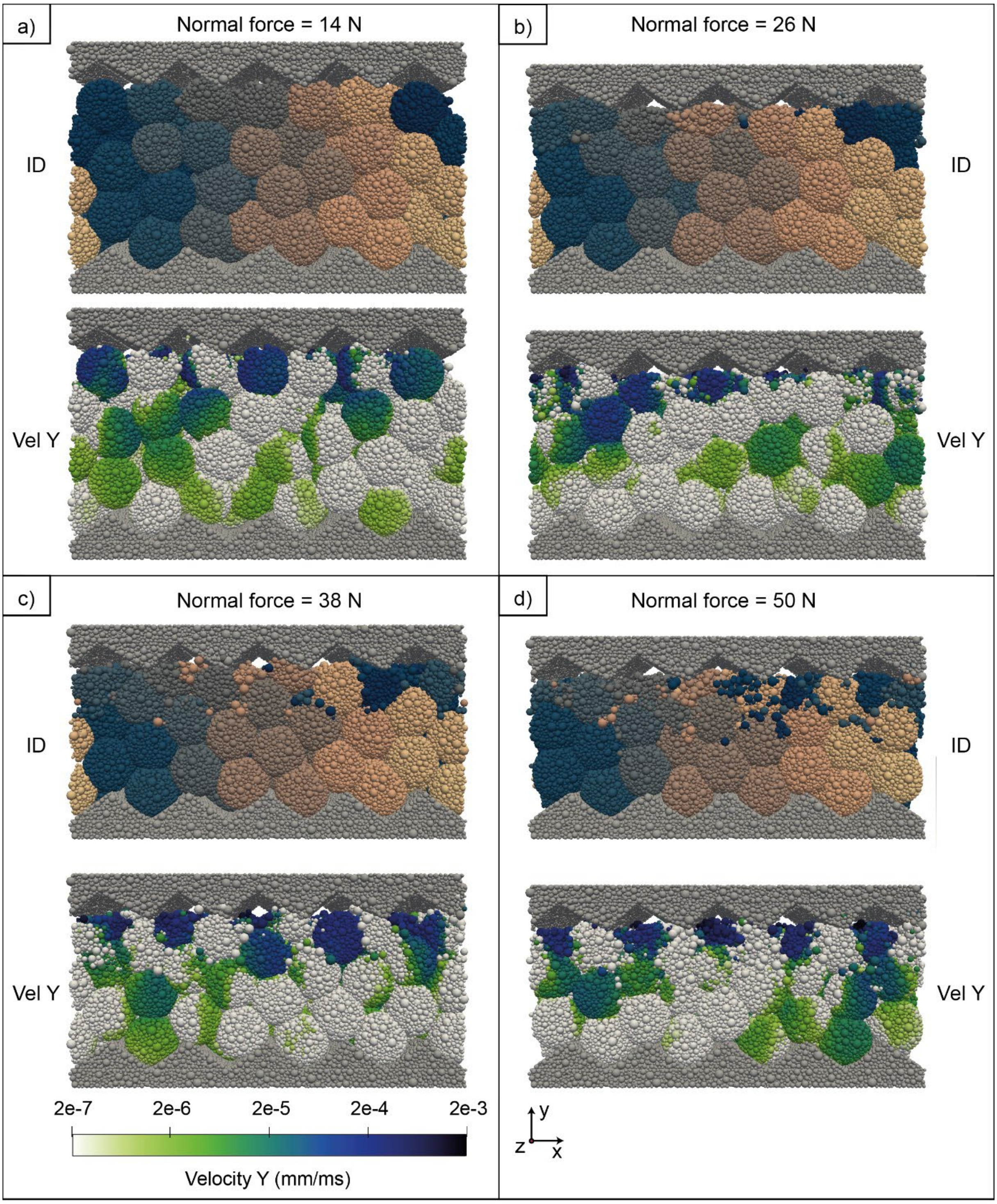

Fig. 5 *Grain ID's (top of each panel) and vertical velocity (bottom of each panel) for models with varying normal force (14-50 N) at the end of each simulation. With increasing normal force, more micro-particles are extracted from their parent grains (ID panels – top). These microparticles are then transported from the moving plate towards the center of the domain. Vertical velocity is the highest close to the moving plate, and it decreases towards the fixed plate. With increasing normal force, the vertical velocity increases with the highest values close to the moving plate*

Fig. 6a shows the number elastic bonds between micro-particles that break during the simulation. All experiments, independent of applied normal force show a distinct change in slope in the number of broken bonds some tens of seconds after the simulation starts. This change reflects the moment the moving plate touches the grains. A second change in slope at round $t = 100\ s$ denotes the moment when the bonded grains, squeezed by the moving plate, finally touch the fixed plate. The third change in slope occurs between $t = 250\ s$ and $t = 350\ s$, which is the time interval between the onset of horizontal shearing at the moving plate and the moment velocity reaches its maximum value (velocity is increased linearly during these $100\ s$). During the first two stages (compaction), the amount of broken bonds is significantly smaller than during shearing. In the final stage, the number of broken bonds slowly approaches the x-axis asymptotically. With increasing normal force, the amount of broken bonds increases. The rate of bond breaking versus shear strain (Fig. 6b) shows that most of the fracturing occurs at the initial stages of shearing and that bond breaking reaches a steady state after the first 5 full rotations (shear strain is equal to 5). Finally, bond breakage is higher at higher normal forces, while the dataset for all normal forces shows episodic spikes in breaking rate.

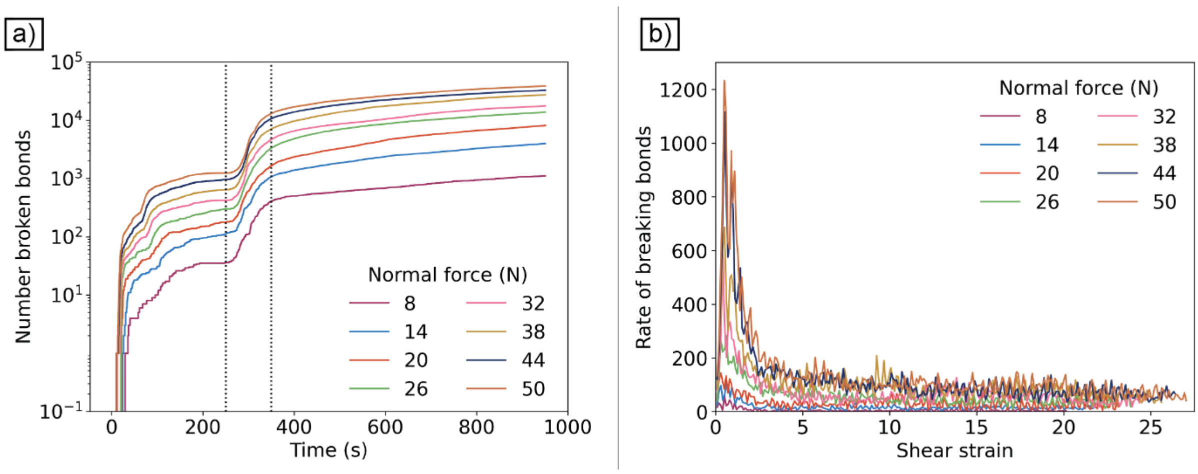

Fig. 6 *a) Number of micro-particle bonds breaking with time, for models with varying normal forces. Y-axis is in logarithmic scale. b) Rate of bond breaking with shear strain for models with varying normal force. Legend shows the normal force for each model (in N) and is the same in both panels*

3.2.2 Force measurements

We measure horizontal force of the models at the fixed plate. Due to the absence of shearing during the initial compaction stage, the horizontal force at the fixed boundary is zero at the beginning of each experiment (Fig. 7a). The second compaction phase is shown by the low-amplitude variation of the horizontal force (left of the first vertical dotted line), while the onset of shearing is clearly visible between 250 – 350 s (between the dotted vertical lines). An increase in the normal force of the model translates to an increase in the horizontal force. In all models, maximum force values are observed at the onset of shearing (Fig. 7a, first vertical line), while after constant shearing is achieved, the horizontal force significantly decreases particularly for lower normal forces. At higher normal forces, the variation in the horizontal force is also larger (Fig. 7a after the second dotted vertical line).

Grain rearrangement and failure are presented in the horizontal force data as force oscillations at different frequencies and amplitudes throughout the simulation. These force oscillations are larger for higher normal forces (Fig. 7a), which results in relatively greater variance values (Fig. 7b). Notably, variance values are larger when calculated using force data from the onset of shearing (first dotted vertical line in Fig. 7a), compared to the variance calculated after full shearing velocity has been achieved (second dotted vertical line in Fig. 7b). This agrees with our observations that most of the bond breakage occurs during the initial stages of shearing (Fig. 6a, b).

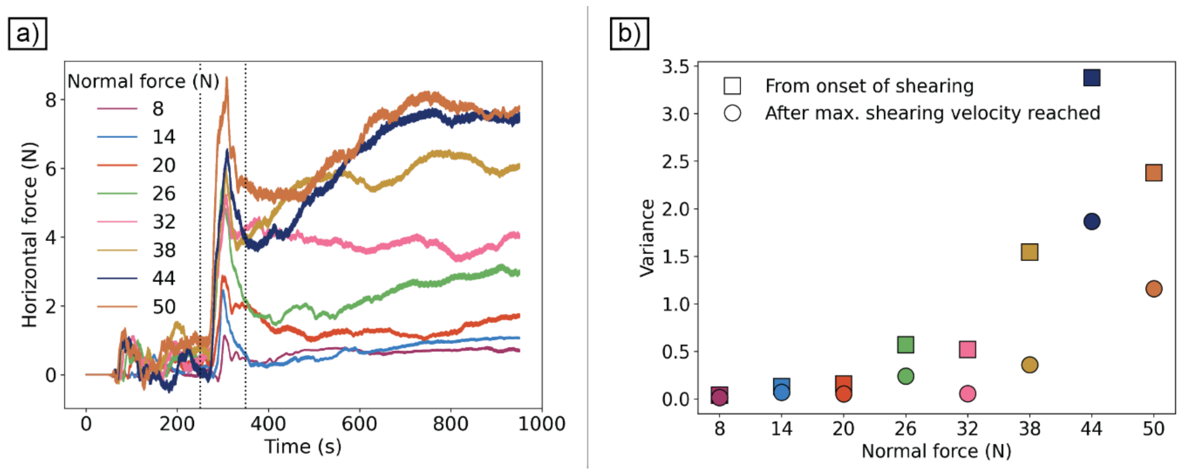

Fig. 7 *a) Horizontal force (in N) measured at the fixed plate, and b) variance of the measured horizontal force at the onset of shearing (square) and after full shearing velocity has been achieved (circles) for models with varying normal force. Legend in a) shows the normal force used for each model (in N) and is the same for both panels*

Finally, to assess the effect of normal force on the overall behavior of the numerical models, we plot the percentage of broken bonds (Fig. 8; black circles) and the maximum recorded horizontal force (Fig. 8; cyan circles) of each model. Increasing normal force results in higher amounts of broken bonds; this in turn results in more fracturing of the grains. In the highest normal force model (50 N), we observe the highest percentage of broken bonds (~12%). Notably, the models with the highest bond breakage and highest horizontal force are also the ones with the largest variance of the horizontal force (Fig. 7b).

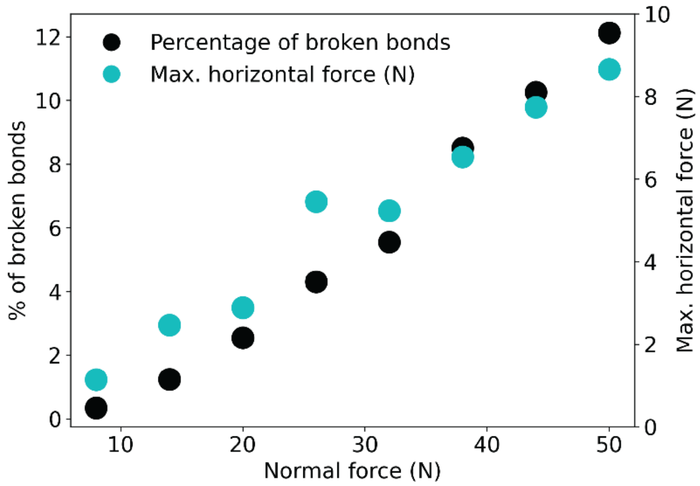

Fig. 8 Percentage of broken bonds (black circles; left vertical axis) and maximum recorded horizontal force in N (cyan circles; right vertical axis), for models with different normal forces (x-axis). The number of interparticle bonds at the beginning of each simulation is ca. 320,000

4 Discussion

4.1 Experiments versus numerical models – limitations

The first difference between the two approaches is the fact that the numerical domain does not take the curvature or the varying shear rate between the inner and outer ring of the experiment into account. Moreover, the laboratory setup has an elastic element between the motor and the force gauge, which is lacking in the numerical setup. Having an elastic element in the experimental boundary condition allows for stick-slip motion to occur. Adding such a spring to the boundary condition of the numerical simulation would have increased the complexity of the system and thus would make the interpretation of the results more difficult. However, the indented plates have an elastic component, given by Young's and shear moduli of the micro-particles forming the plates (which is the same as those of the micro-particles forming the grains), while we ensure that the plates remain unbreakable by using an increased cohesion (25 times that of the micro-particles forming the grains).

The indentations of the numerical plates have the same height as those in the laboratory experiments, but their shape differs. However, the chosen elongated pyramid shape for the numerical models has been used in previous simulations (e.g., Abe and Mair, 2009; Mair and Abe, 2011; Rathbun et al., 2013). Nonetheless, previous studies showed that the shape and size of the rigid plate indentations (roughness) plays a role in the grain comminution (Mair and Abe, 2011), the critical displacement (Abe et al., 2002), and mechanical coupling (Rathbun et al., 2013). Therefore, future work would include a more detailed study on how the shape of the indentations affects our numerical results.

In the experiments, normal force and shearing are applied at different boundaries of the apparatus, while horizontal force is measured at the moving boundary. Nonetheless, because of gravity and the fact that the walls of the experimental chamber are moving with the bottom boundary, deformation localizes at the stationary boundary in the analog experiments (top). In the numerical models, we impose both normal force and shearing at the same (moving) plate, while we measure the horizontal forces at the fixed plate, away from the shear zone, like in the experiments. This overall shearing behavior is common both in laboratory experiments of granular shear at low stress and high strain rates (e.g., Pouliquen and Gutfraind, 1996; Veje et al., 1999; Losert et al., 2000; Mueth et al., 2000; Bocquet et al., 2002), as well as in 2D (Aharonov and Sparks, 2002) and 3D numerical models (Mair and Hazzard,2007; Rathbun et al. 2013).

Another difference between the experimental and the numerical setup is the high-density approximation used in the numerical models. Because the minimum stable numerical timestep depends on particle density, a very small density, such as that of the HydroOrbs, would result in a very small stable timestep, which in turn would make the numerical computation too expensive. This is a common issue in the DE method, and one way to counter it is by using much higher densities (several orders of magnitudes larger). However, larger densities generally result in inaccurate accelerations. Thus, for the high-density approximation to not influence the overall deformation, a penalty factor is introduced (a dampening of the particle kinetic energy; Cundall and Strack, 1979). This factor is causing the right-hand-side of the equation $F = ma$ to approach zero. In principle, we are approximately solving the remaining $F = 0$ differential equation, i.e., the steady-state solution of the system of equations comprising the DE simulation. Because the density is not infinite (accelerations do not equal zero), the DE solution will be “quasi”-static rather than steady state. Since the laboratory experiments were conducted under quasi-static conditions, by employing the high-density approximation with the penalty factor, we maintain realistic deformation rates in the model. The use of this approximation is further facilitated by the absence of gravity, since a very large density would result in a very large acceleration. Therefore, in combination with the absence of gravity and an artificial dampening of the kinetic energy of the particles, this approach allows for faster computations.

4.2 Grain re-arrangement and failure

To compare the results between the analog and numerical experiments, we plot the percentage of broken grains observed in each model versus the equivalent normal stress (Fig. 9). Not surprisingly, an increase in normal force results in an increase in the number of grains that break in both approaches. The small discrepancy between the percentage of broken bonds (Fig. 8a) and the percentage of broken grains in the numerical models (Fig. 9) can be attributed to the fact that a single bond breaking from a grain results in this grain being considered broken. Since there are multiple orders of magnitude fewer grains than bonds (116 versus ~320000), this leads to higher percentages of broken grains. To dampen this effect, we consider a grain broken after it has lost 10% of its mass.

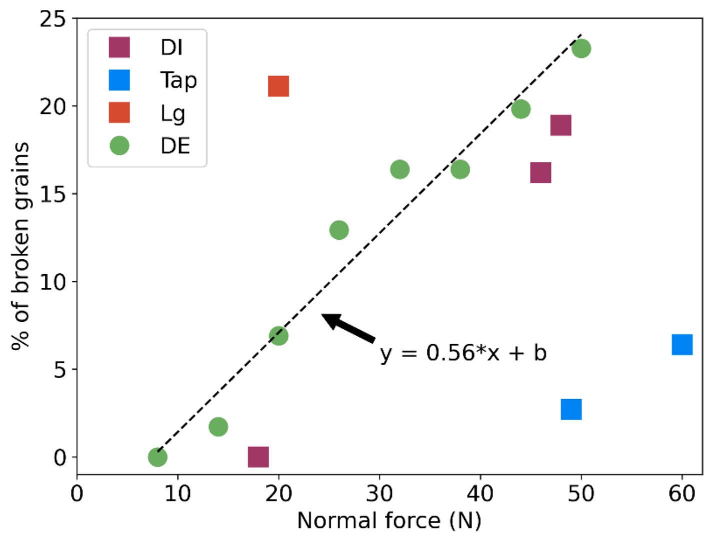

Fig. 9 *Percentage of broken grains with increasing normal force in analog (squares) and numerical models (circles). The slope of the curve y = ax + b is a=0.56, where x is the normal force and y the percentage of broken grains. DI: orbs immersed in de-ionized water, Tap: orbs immersed in tap water, Lg: large orbs immersed in tap water, DE: discrete element grains*

We can fit the results of the broken grains with normal force of the numerical models (Fig. 9, circles) using a linear regression of the form y = ax +b, where *y* is the percentage of broken grains, a = 0.53 and *x* is the normal force. Because the numerical models are calibrated based on the dimensions and materials parameters of the DI experiments, we exclude all the other experiments from the fitting (blue and orange squares, respectively). We interpret the difference in the results of the excluded models to reflect the effect of grain size. The physical experiments show that with an increase in orb size the percentage of broken orbs also increases regardless of normal force. This observation is in line with previous findings showing that grain size plays an important role in the macroscopic behavior of a fault gouge (e.g., Anthony and Marone, 2005). One potential explanation for the different behavior of the smaller HydroOrbs is that smaller HydroOrbs made with tap water may be able to rearrange and roll or slide past other orbs to fit into void spaces more readily than larger orbs such as those made with DI water and the large colorful orbs.

In the physical experiments, migration of orb fragments is observed from the top of the model, where shearing is imposed, towards the middle of the experimental chamber. Typically, the orb fragments stop a few centimeters above the bottom plate, where they create a band of fragments in the middle of the experimental chamber (Fig. 1 and 2, Table 2). The thickness of the fragment band increases throughout the experiment as more orbs break at the top of the chamber, and then decreases when the fragment supply from near the top of the experiment stops. Throughout the numerical models, we observe bond breakage and then migration of the unbound micro-particles from the moving plate/shear boundary toward the middle of the model domain. Similar to the physical experiments, the numerical microparticles move to areas with higher porosity between the grains (Siman-Tov and Brodsky, 2018) (Fig. 4b, c, d), while most grain fragments do not move past the middle of the grain layer.

Experimental, numerical, and theoretical investigations of dense granular systems show that grain size segregation can occur due to gradients in the shear rates (e.g., Stephens & Bridgwater, 1978; Fran & Hill, 2011; Gray & Thornton, 2005; May et al., 2010). This "kinetic sieving" allows smaller particles (grain fragments) to fill voids created by larger particles (whole grains) and lever large particles upwards (Gray & Thornton, 2005; Fran & Hill, 2011). Kinetic sieving in the presence of a shear strain rate difference may result in larger-unbroken orbs moving towards the area of the highest shear strain while smaller fragments move downwards (Stephens & Bridgwater, 1978; Fran & Hill, 2011). Downward fragment migration may therefore halt when no voids are opened from the movement of the whole grains (little orb/grain movement at the boundary far from the shearing zone in the experimental and numerical domains). Kinetic sieving is, therefore, independent of gravity and could potentially explain the movement of the numerical microparticles in the absence of gravity in the numerical simulations.

The numerical results suggest that bond (and hence grain) breakage occurs in episodic pulses, which becomes significantly smaller after a shear strain of 1-3 is achieved (Fig. 6b). Similar findings by Abe and Mair (2005) and Mair and Abe (2008; 2011) regarding episodic spikes in the bond breakage rate versus strain curves suggest short-lived periods of enhanced bond breakage during their simulations. These periods may represent aggregate grains breaking apart through mechanisms such as avalanches or zipper-type processes (Abe and Mair, 2005). A gradual decrease in bond breakage rate with accumulated strain was also reported after reaching a strain of 1 (Mair and Abe, 2008). Friction controls the type of motion of particles (e.g., rolling vs. sliding). Particles with high friction move by rolling, while particles with low friction prefer a combination of rolling, sliding, and distribution of shear (Makedonska et al., 2011). Since the grains in the numerical models and the experiments have a very low friction, we expect that they also deform via a combination of those movements. Finally, Rathbun et al (2013) calculated the effect of particle friction on the strength of the gouge and demonstrated that with increasing particle friction, the overall strength of the gouge also increases. Therefore, the physical and hence the numerical experiments correspond to a weak gouge.

4.3 Effect of normal force

In both physical and numerical simulations, we observe an increase in broken bonds with increasing normal force. These results agree with the observations by Abe and Mair (2005) and Mair and Abe (2008), who report an increase in fracturing with increasing normal force during their 3D numerical simulations. Additionally, the maximum recorded horizontal force increases (Fig. 7a and 8) with an increase in normal force. The observed force fluctuation with time (Fig. 7a) is smaller for models with a low normal force. This potentially indicates that the granular system flows continuously, since it is unable to sustain the applied shear stress (Arcangelis et al., 2011). In the numerical simulations, peak horizontal forces (Fig. 7a) coincide with the steepest curve in the broken bond curves (Fig. 6a), while post-peak forces fluctuate and the rate of breaking of bonds is almost constant (Fig. 6b). The dramatic drop in horizontal force corresponds mainly to grain fracturing while post-peak fluctuations reflect increased grain rearrangement. The same behavior can be observed in the physical experiments, where breaking of the orbs leads to a decrease in variance and total force (Fig. 3). Most orb failure occurs toward the beginning of the analog experiments where the steepest decrease in pulling force and variance are observed (Fig. 3). In the numerical experiments the maximum rate of bond breakage indicating orb failure also occurs at the beginning of shearing (Fig. 6b).

The variance (average fluctuation of the pulling force) in the physical experiments reaches a relatively steady value after the initial drop in every experiment. In contrast, where no orb failure occurs (experiment CL_D1), the total force and variance values are relatively constant throughout the experiment while recording only orb rearrangement. These observations agree with Wu et al. (2022) who found that in post-peak stress-displacement curves, a dramatic stress drop is due to rock fragment crushing, and the moderate decline indicates grain rotation. The variance of the horizontal force in the numerical experiments is higher for high values of normal force; this suggests an increased bond and grain breakage for those models.

5 Conclusions

We introduced a new elasto-plastic material, HydroOrbs, that has the ability to fracture and can be used to investigate grain comminution in granular media under simple shear conditions. Physical experiments using HydroOrbs showed a clear dependency of grain comminution on normal force when experimenting with orbs of the same size, as well as on grain size when normal force is kept relatively constant. We used these physical experiments to benchmark DE models of elasto-plastic grains that can move, rotate, and fracture under simple shear conditions. The DE models are able to qualitatively reproduce both grain comminution and horizontal force fluctuations observed during the physical experiments. The successful reproduction of the experimental results with the DE formulation will allow for the use of these numerical models to investigate parameter spaces that are inaccessible for experiments such as the impact of internal friction and cohesion on deformation of granular systems.

6 Appendix

Table 3 Supplemental table for analog experiments. Summary table of HydroOrb Properties. One standard deviation listed after ± symbol.

	Colorless HydroOrbs		Colorful HydroOrbs		
HydroOrb Property	**DI Water**	**Tap Water**	**DI Water**	**Tap Water**	**Large Orbs**
Size / Diameter (cm)	1.69 ± 0.09	1.41 ± 0.06	1.66 ± 0.08	1.43 ± 0.08	3.87 ± 0.25
Volume (cm^3)	2.55 ± 0.44	1.47 ± 0.19	2.43 ± 0.34	1.54 ± 0.30	31.76 ± 8.27
Mass (g)	2.88 ± 0.29	1.76 ± 0.14	2.46 ± 0.34	1.71 ± 0.18	38.12 ± 11.27
Density (g/cm^3)	1.06 ± 0.06	1.09 ± 0.08	1.07 ± 0.05	1.07 ± 0.07	1.04 ± 0.06
Poisson's Ratio	0.41 ± 0.08	0.20 ± 0.05	0.38 ± 0.06	0.33 ± 0.06	0.37 ± 0.07
Young's Modulus (kPa)	136.88 ± 67.64	197.00 ± 97.68	107.55 ± 41.03	91.47 ± 33.12	43.68 ± 23.16
Shear Modulus (kPa)	48.54 ± 23.99	81.29 ± 41.29	37.80 ± 16.08	34.65 ± 12.54	16.78 ± 8.55
Yield Force (N)					
Non-punctured	21.40 ± 4.03	20.53 ± 5.31	-	-	27.30 ± 12.13
Punctured	5.09 ± 2.63	3.98 ± 2.53	4.89 ± 2.96	3.56 ± 2.42	9.52 ± 4.15
Area of Force Application (cm^2)					
Non-punctured	2.96 ± 0.54	2.61 ± 0.28	-	-	18.07 ± 6.20
Punctured	2.00 ± 0.37	1.86 ± 0.29	1.91 ± 0.37	1.62 ± 0.36	13.47 ± 5.21
Yield Stress (kPa)					
Non-punctured	72.27 ± 18.86	78.55 ± 21.93	-	-	15.01 ± 14.37
Punctured	25.44 ± 13.96	21.43 ± 13.81	25.62 ± 16.27	21.97 ± 15.70	7.07 ± 12.79

7 References

Abe, S., Dieterich, J. H., Mora, P., & Place, D. (2002). Simulation of the Influence of Rate- and State-dependent Friction on the Macroscopic Behavior of Complex Fault Zones with the Lattice Solid Model. *Pure and Applied Geophysics*, 159(9), 1967–1983. https://doi.org/10.1007/s00024-002-8718-7

Abe, S., & Mair, K. (2009). Effects of gouge fragment shape on fault friction: New 3D modelling results. *Geophysical Research Letters*, 36(23), L23302. https://doi.org/10.1029/2009GL040684

Abe, S., & Mair, K. (2005). Grain fracture in 3D numerical simulations of granular shear. *Geophysical Research Letters*, 32(5), L05305. https://doi.org/10.1029/2004GL022123

Abe, S., Place, D., & Mora, P. (2004). A Parallel Implementation of the Lattice Solid Model for the Simulation of Rock Mechanics and Earthquake Dynamics. *Pure and Applied Geophysics*, 161(11–12), 2265–2277. https://doi.org/10.1007/s00024-004-2562-x

Aharonov, E., & Sparks, D. (2002). Shear profiles and localization in simulations of granular materials. *Physical Review E*, 65(5), 051302. https://doi.org/10.1103/PhysRevE.65.051302

Anthony, J. L. (2005). Influence of particle characteristics on granular friction. *Journal of Geophysical Research*, 110(B8), B08409. https://doi.org/10.1029/2004JB003399

Arcangelis, L. de, Ciamarra, M. P., Lippiello, E., & Godano, C. (2011). Micromechanics and statistics of slipping events in a granular seismic fault model. *Journal of Physics: Conference Series*, 319(1), 012001. https://doi.org/10.1088/1742-6596/319/1/012001

Birren, T., & Reber, J. E. (2019). The Impact of Rheology on the Transition From Stick-Slip to Creep in a Semibrittle Analog. *Journal of Geophysical Research: Solid Earth*, 124(3), 3144–3154. https://doi.org/10.1029/2018JB016914

Bocquet, L., Losert, W., Schalk, D., Lubensky, T. C., & Gollub, J. P. (2001). Granular shear flow dynamics and forces: Experiment and continuum theory. *Physical Review E*, 65(1), 011307. https://doi.org/10.1103/PhysRevE.65.011307

Brace, W. F., & Byerlee, J. D. (1966). Stick-Slip as a Mechanism for Earthquakes. *Science*, 153(3739), 990–992. https://doi.org/10.1126/science.153.3739.990

Cain, R. G., Page, N. W., & Biggs, S. (2001). Microscopic and macroscopic aspects of stick-slip motion in granular shear. *Physical Review E*, 64(1), 016413. https://doi.org/10.1103/PhysRevE.64.016413

Cates, M. E., Wittmer, J. P., Bouchaud, J.-P., & Claudin, P. (1998). Jamming, Force Chains, and Fragile Matter. *Physical Review Letters*, 81(9), 1841–1844. https://doi.org/10.1103/PhysRevLett.81.1841

Chang, S., Kim, M., Oh, S., Min, J. H., Kang, D., Han, C., Ahn, T., Koh, W.-G., & Lee, H. (2018). Multi-scale characterization of surface-crosslinked superabsorbent polymer hydrogel spheres. *Polymer*, 145, 174–183. https://doi.org/10.1016/j.polymer.2018.04.073

Cundall, P. A., & Strack, O. D. L. (1979). A discrete numerical model for granular assemblies. *Géotechnique*, 29(1), 47–65. https://doi.org/10.1680/geot.1979.29.1.47

Daniels, K. E., & Hayman, N. W. (2008). Force chains in seismogenic faults visualized with photoelastic granular shear experiments. *Journal of Geophysical Research*, 113(B11), B11411. https://doi.org/10.1029/2008JB005781

Dijksman, J. A., Brodu, N., & Behringer, R. P. (2017). Refractive index matched scanning and detection of soft particles. *Review of Scientific Instruments*, 88(5), 051807. https://doi.org/10.1063/1.4983047

Fan, Y., & Hill, K. M. (2011). Theory for shear-induced segregation of dense granular mixtures. New Journal of Physics, 13. https://doi.org/10.1088/1367-2630/13/9/095009

Frye, K. M., & Marone, C. (2002). The effect of particle dimensionality on Granular friction in laboratory shear zones. *Geophysical Research Letters*, 29(19), 22-1-22–24. https://doi.org/10.1029/2002GL015709

Gray, J. M. N., & Thornton, A. (2005). A theory for particle size segregation in shallow granular free-surface flows. *Proceedings of the Royal Society A: Mathematical, Physical and Engineering Sciences*, 461(2057), 1447–1473. https://doi.org/10.1098/rspa.2004.1420

Guo, Y., & Morgan, J. K. (2006). The frictional and micromechanical effects of grain comminution in fault gouge from distinct element simulations. *Journal of Geophysical Research: Solid Earth*, 111(B12), n/a-n/a. https://doi.org/10.1029/2005JB004049

James, J. D., Ludwick, J. M., Wheeler, M. L., & Oyen, M. L. (2020). Compressive failure of hydrogel spheres. *Journal of Materials Research*, 35(10), 1227–1235. https://doi.org/10.1557/jmr.2020.114

Ladd, C. R., & Reber, J. E. (2020). The Effect of a Liquid Phase on Force Distribution During Deformation in a Granular System. *Journal of Geophysical Research: Solid Earth*, 125(8), 1–17. https://doi.org/10.1029/2020JB019771

Losert, W., Bocquet, L., Lubensky, T. C., & Gollub, J. P. (2000). Particle Dynamics in Sheared Granular Matter. *Physical Review Letters*, 85(7), 1428–1431. https://doi.org/10.1103/PhysRevLett.85.1428

Mair, K., & Abe, S. (2011). Breaking Up: Comminution Mechanisms in Sheared Simulated Fault Gouge. *Pure and Applied Geophysics*, 168(12), 2277–2288. https://doi.org/10.1007/s00024-011-0266-6

Mair, K., & Abe, S. (2008). 3D numerical simulations of fault gouge evolution during shear: Grain size reduction and strain localization. *Earth and Planetary Science Letters*, 274(1–2), 72–81. https://doi.org/10.1016/j.epsl.2008.07.010

Mair, K., Frye, K. M., & Marone, C. (2002). Influence of grain characteristics on the friction of granular shear zones. *Journal of Geophysical Research: Solid Earth*, 107(B10), ECV 4-1-ECV 4-9. https://doi.org/10.1029/2001JB000516

Mair, K., & Hazzard, J. F. (2007). Nature of stress accommodation in sheared granular material: Insights from 3D numerical modeling. *Earth and Planetary Science Letters*, 259(3–4), 469–485. https://doi.org/10.1016/j.epsl.2007.05.006

Makedonska, N., Sparks, D. W., Aharonov, E., & Goren, L. (2011). Friction versus dilation revisited: Insights from theoretical and numerical models. *Journal of Geophysical Research*, 116(B9), B09302. https://doi.org/10.1029/2010JB008139

Marone, C., & Scholz, C. H. (1989). Particle-size distribution and microstructures within simulated fault gouge. *Journal of Structural Geology*, 11(7), 799–814. https://doi.org/10.1016/0191-8141(89)90099-0

May, L. B. H., Golick, L. A., Phillips, K. C., Shearer, M., & Daniels, K. E. (2010). Shear-driven size segregation of granular materials: Modeling and experiment. *Physical Review E - Statistical, Nonlinear, and Soft Matter Physics*, 81(5). https://doi.org/10.1103/PhysRevE.81.051301

McLafferty, S., Bix, H., Bogatz, K., & Reber, J. E. (2022). New ring shear deformation apparatus for three-dimensional multiphase experiments: First results. *EGUsphere*, October 1–21. https://doi.org/doi.org/10.5194/egusphere-2022-1004

Mora, P., & Place, D. (1994). Simulation of the frictional stick-slip instability. *Pure and Applied Geophysics*, 143(1–3), 61–87. https://doi.org/10.1007/BF00874324

Mora, P., & Place, D. (1993). A lattice solid model for the nonlinear dynamics of earthquakes. *International Journal of Modern Physics C*, 04(06), 1059–1074. https://doi.org/10.1142/S0129183193000823

Mora, P., & Place, D. (1998). Numerical simulation of earthquake faults with gouge: Toward a comprehensive explanation for the heat flow paradox. *Journal of Geophysical Research: Solid Earth*, 103(B9), 21067–21089. https://doi.org/10.1029/98JB01490

Morgan, J. K., & Boettcher, M. S. (1999). Numerical simulations of granular shear zones using the distinct element method: 1. Shear zone kinematics and the micromechanics of localization. *Journal of Geophysical Research: Solid Earth*, 104(B2), 2703–2719. https://doi.org/10.1029/1998JB900056

Mueth, D. M., Debregeas, G. F., Karczmar, G. S., Eng, P. J., Nagel, S. R., & Jaeger, H. M. (2000). Signatures of granular microstructure in dense shear flows. *Nature*, 406(6794), 385–389. https://doi.org/10.1038/35019032

Place, D., & Mora, P. (1999). The Lattice Solid Model to Simulate the Physics of Rocks and Earthquakes: Incorporation of Friction. *Journal of Computational Physics*, 150(2), 332–372. https://doi.org/10.1006/jcph.1999.6184

Pouliquen, O., & Gutfraind, R. (1996). Stress fluctuations and shear zones in quasistatic granular chute flows. *Physical Review E*, 53(1), 552–561. https://doi.org/10.1103/PhysRevE.53.552

Rathbun, A. P., Renard, F., & Abe, S. (2013). Numerical investigation of the interplay between wall geometry and friction in granular fault gouge. *Journal of Geophysical Research: Solid Earth*, 118(3), 878–896. https://doi.org/10.1002/jgrb.50106

Reber, J. E., Hayman, N. W., & Lavier, L. L. (2014). Stick-slip and creep behavior in lubricated granular material: Insights into the brittle-ductile transition. *Geophysical Research Letters*, 41(10), 3471–3477. https://doi.org/10.1002/2014GL059832

Reber, J. E., Lavier, L. L., & Hayman, N. W. (2015). Experimental demonstration of a semi-brittle origin for crustal strain transients. *Nature Geoscience*, 8(9), 712–715. https://doi.org/10.1038/ngeo2496

Shojaaee, Z., Brendel, L., Török, J., & Wolf, D. E. (2012). Shear flow of dense granular materials near smooth walls. II. Block formation and suppression of slip by rolling friction. *Physical Review E*, 86(1), 011302. https://doi.org/10.1103/PhysRevE.86.011302

Sibson, R. H. (1977). Fault rocks and fault mechanisms. *Journal of the Geological Society*, 133(3), 191–213. https://doi.org/10.1144/gsjgs.133.3.0191

Siman-Tov, S., & Brodsky, E. E. (2018). Gravity-Independent Grain Size Segregation in Experimental Granular Shear Flows as a Mechanism of Layer Formation. *Geophysical Research Letters*, 45(16), 8136–8144. https://doi.org/10.1029/2018GL078486

Stephens, D. J., & Bridgwater, J. (1978). The mixing and segregation of cohesionless particulate materials part II. Microscopic mechanisms for particles differing in size. *Powder Technology*, 21(1), 29–44. https://doi.org/10.1016/0032-5910(78)80105-3

Veje, C. T., Howell, D. W., & Behringer, R. P. (1999). Kinematics of a two-dimensional granular Couette experiment at the transition to shearing. *Physical Review E*, 59(1), 739–745. https://doi.org/10.1103/PhysRevE.59.739

Wang, Y., Abe, S., Latham, S., & Mora, P. (2006). Implementation of Particle-scale Rotation in the 3-D Lattice Solid Model. *Pure and Applied Geophysics*, 163(9), 1769–1785. https://doi.org/10.1007/s00024-006-0096-0

Wu, L., Chen, G., Xing, J., & Lin, Z. (2022). Brittle cataclastic process of fault rocks based on a large-displacement direct shear model realized with DEM. *Journal of Structural Geology*, 161, 104641. https://doi.org/10.1016/j.jsg.2022.104641

8 Statements and Declarations

Funding

P.I. Ioannidi, S. McLafferty, J.E. Reber, and G. Morra have been supported through National Science Foundation CAREER award #1843676.

Competing Interests

The authors have no relevant financial or non-financial interests to disclose.

Author Contributions

Conceptualization: J.E.R, G.M., P.I.I.; Methodology: J.E.R, D.W, P.I.I.; Formal analysis and investigation: P.I.I., S.McL., J.E.R., G.M.; Writing – original draft preparation: P.I.I., S. McL., J.E.R.; Writing – review and editing: P.I.I., J.E.R; Funding acquisition: J.E.R.; Resources: J.E.R., G.M., D.W.; Supervision: J.E.R., G.M. All authors reviewed the manuscript.